

BaFe₂Se₃ a quasi-unidimensional non-centrosymmetric superconductor

S. Deng^{*,1,2} A. Roll^{*,3,4} W. G. Zheng^{*,3} G. Giri^{2,5} T. Vasina² D. Bounoua⁴ P. Fertey⁶ M. Verseils⁶
C. Bellin⁷ A. Forget⁸ D. Colson⁸ P. Foury-Leykian³ M.B. Lepetit^{9,2} and V. Balédent^{3,10}

^{1*}These authors contributed equally to this work.

²Institut Laue Langevin, 38000 Grenoble, France

³Université Paris-Saclay, CNRS, Laboratoire de Physique des Solides, 91405, Orsay, France.

⁴Université Paris-Saclay, CNRS-CEA, Laboratoire Léon Brillouin, 91191, Gif sur Yvette, France

⁵Current address: Physics Dept., VIT Bhopal University, Bhopal, India

⁶Synchrotron SOLEIL, L'Orme des Merisiers, Saint Aubin BP 48, 91192, Gif-sur-Yvette, France

⁷Université Pierre et Marie Curie, IMPMC, CNRS UMR7590, 4 Place Jussieu, 75005 Paris, France

⁸Université Paris-Saclay, CEA, CNRS, SPEC, 91191, Gif-sur-Yvette, France.

⁹Institut Néel, CNRS, 38042 Grenoble, France

¹⁰Institut universitaire de France (IUF)*

(Dated: February 20, 2026)

The spin-ladder compounds of the BaFe₂X₃ (X = chalcogen) family may be viewed as dimensional reductions—along stripe-like motifs—of the two-dimensional iron-based pnictide planes extensively studied since 2006. Remarkably, despite their reduced dimensionality, these materials retain the capacity for unconventional ground states, exemplified by the emergence of superconductivity in BaFe₂Se₃ under applied pressure beyond 10 GPa, following a structural phase transition at 4 GPa. Here, we report a comprehensive investigation combining high-resolution single-crystal X-ray diffraction, infrared spectroscopy, and *ab initio* calculations, which together elucidate the true crystallographic nature of this pressure-induced superconducting phase. While X-ray diffraction alone reveals a symmetry lowering from the widely accepted orthorhombic *Cmcm* group to a monoclinic structure, it lacks sufficient sensitivity to resolve the precise space group. By integrating vibrational spectroscopy with density functional theory, we provide unambiguous evidence that the high-pressure phase is non-centrosymmetric, adopting the polar space group *P2₁*. These findings not only revise the structural assignment of BaFe₂Se₃ in its superconducting state but also establish its non-centrosymmetric character—an essential ingredient for potential unconventional pairing mechanisms—thereby opening new perspectives on the interplay between lattice symmetry, dimensionality, and superconductivity in iron-based materials.

Unconventional superconductivity remains one of the most emblematic quantum properties in solid-state physics, resisting any consensus on a phenomenological or microscopic model [1–3]. Initiated by the discovery of high-critical temperature cuprates, this pursuit of elevated temperatures has led to the exploration of new materials such as iron-based pnictides, heavy fermion compounds, and more recently, nickelates [4]. While the mechanism behind Cooper pair formation in these families remains elusive, there is a broad consensus that understanding superconductivity requires investigating phases and orders neighboring the superconducting dome [5, 6]. Indeed, to elucidate pairing mechanisms or test proposed models, it is pertinent to observe the presence of competing or intertwined order parameters. This has been done in particular in numerous quasi-two-dimensional (2D) iron-based superconductors such as FeSe or BaFe₂As₂, whose square-lattice planes and layered architectures have been extensively studied both structurally and magnetically [4, 7–10]. These studies have revealed how structural and magnetic degrees of freedom, often intimately linked, evolve upon approaching the superconducting dome via chemical doping or applied pressure. Recently, new spin-ladder iron-based systems have demonstrated superconductivity under pressure. With a general formula of BaFe₂X₃ (X=S and Se),

they represent the first quasi-one-dimensional iron-based superconductors devoid of a square-lattice motif [11, 12]. The quasi-one-dimensional character of these compounds originates from their two-leg ladder crystal structure and is reflected in strongly anisotropic transport properties and low-dimensional magnetic correlations [12–15]. In this context, these two compounds offer a unique opportunity to investigate how reducing dimensionality from 2D to 1D affects the delicate balance between magnetism, structure, and superconductivity.

Consisting of two iron ladders per unit cell, the BaFe₂Se₃ and BaFe₂S₃ compounds were respectively reported to crystallize in the *Pnma* and *Cmcm* space groups [16]. In the *Cmcm* structure, the ladders, formed by edge-sharing FeX₄ tetrahedra along the *c* axis, are perfectly contained in the (*a,c*) plane, whereas a tilt is observed in *Pnma*. Interestingly, BaFe₂Se₃ is reported to undergo a transition from *Pnma* to *Cmcm* above 3–4 GPa [17], suggesting a common atomic structure between the two compounds close to the superconducting phase. This apparent universality of the neighboring phases of the superconducting dome is reinforced by the presence of the same magnetic order, as measured by neutron diffraction under pressure [18]. However, a more thorough investigation on single crystals of BaFe₂Se₃, utilizing X-ray diffraction, infrared spectroscopy, and *ab-*

ab-initio calculations, revealed that the actual space group at ambient pressure is Pm , a significantly lower symmetry than the previously reported average $Pnma$ space group [19, 20]. Understanding the symmetries at play in these compounds is therefore crucial for comprehending their physical properties, especially since such symmetry breaking can endow BaFe_2Se_3 with multiferroic behavior. An even more intriguing possibility is that the loss of inversion symmetry persists into the superconducting phase, placing BaFe_2Se_3 within the rare class of non-centrosymmetric superconductors [21–23].

Until now, very limited information has been available regarding the crystallographic structure of the superconducting phase itself, despite its crucial importance for understanding the nature of superconductivity in this system. In light of the ambient-pressure results, it is therefore essential to investigate the structure of BaFe_2Se_3 in single crystals under combined high-pressure and low-temperature conditions. In this Letter, we present a study of BaFe_2Se_3 under pressure, combining X-ray diffraction (XRD), infrared (IR) and Raman spectroscopies, and *ab-initio* calculations. Our results reveal that the high-pressure space group of BaFe_2Se_3 in the phase where superconductivity emerges is $P2_1$. This symmetry establishes BaFe_2Se_3 as one of the very few known examples of a quasi-one-dimensional non-centrosymmetric superconductor.

Experimental methods. Single crystals of BaFe_2Se_3 were grown using the self-flux method as described in Ref. [19]. We emphasize that the samples used in this study originate from the same batch that was extensively characterized in previous works. Compositional uniformity was verified by energy-dispersive X-ray spectroscopy (EDX), showing a nominal stoichiometry within 2% uncertainty (see SI of Ref. [19]), and scanning electron microscopy (SEM) confirmed the absence of structural defects at the microscale [24]. Although structural symmetry, particularly non-centrosymmetry, can be sensitive to stoichiometry and sample quality, no deviation from the reported superconducting composition or structure was detected. Despite the absence of low-temperature resistivity measurements under pressure showing superconductivity, we are confident that the observed non-centrosymmetric structure corresponds to a superconducting phase representative of this material family. For each experiment, one or several single crystals of BaFe_2Se_3 were loaded in a membrane-driven diamond anvil cell (DAC), using a stainless steel gasket with pressure transmitting media adapted to each technique (see details in the Supplementary Information (SI) [25]). The pressure inside the diamond anvil cell was measured using the ruby fluorescence technique, yielding a 5% relative accuracy on the pressure value [26]. XRD and IR reflectivity were performed on the CRISTAL and AILES beamline respectively, at synchrotron SOLEIL. Due to technical constraints associated with the cryostat used for

measurements in diamond anvil cells required for high-pressure experiments, the lowest temperatures achieved were not identical across techniques: 10 K for diffraction measurements and 50 K for infrared spectroscopy. However, as shown in our previous work at ambient pressure [20], phonon energies exhibit minimal variation between 50 K and 10 K.

Raman scattering experiments were performed at IMPMC (Paris) using a 534 nm laser source with a fixed power of 80 mW in a backscattering geometry. Measurements were carried out at 300 K, as the Raman signal is particularly weak in this family of compounds already at ambient conditions, consistent with previous reports [27], preventing us to measure at both low temperature and high pressure despite several attempts. Polarized Raman spectra were successfully measured under pressure using well-defined scattering geometries, expressed in Porto notation as (a, a) and (c, c) configurations, where both incident and scattered electric fields are aligned along the crystallographic \mathbf{a} and \mathbf{c} directions, respectively (in $Cmcm$ notation).

The *ab-initio* calculations were done using Density Functional Theory (DFT). In order to best account for the electronic correlation at the Fermi level, we used the hybrid B3LYP functional [28] and a localized basis set. An atomic gaussian basis of $3\zeta + P$ quality was used for the Fe and Se atoms [29]. The Ba atoms were represented using a relativistic core pseudo-potential of the Stuttgart group [30] and the associated basis set where the diffuse functions exponents were taken as 1.2 as recommended by Scuseria *et al* [31]. The calculations were done using the CRYSTAL23 code [32]. The shrinking factor was set to $8 \times 12 \times 4$ resulting in a sampling net of 126 \mathbf{k} -points. The stripe spin ordering found in neutron scattering experiments of BaFe_2Se_3 under pressure [18] was used in all calculations.

X-ray diffraction. The most comprehensive study of structural properties in this compound is provided in Ref. 17, where room temperature X-Ray data under pressure up to 50 GPa are provided. Between 0 – 3.5 GPa, V. Svitlyk *et al* propose a $Pnma$ space group, between 3.5 – 16.6 GPa a $Cmcm$ group and above 16.6 GPa an isostructural $Cmcm$ phase where the \mathbf{b} axis collapses while the \mathbf{a} and \mathbf{c} ones expand [17].

One should however remember that in these compounds diffraction measurements often lead to average structures, rather than true space groups. Indeed, while at ambient pressure X-Ray were suggesting a $Pnma$ group [16, 17], our high resolution X-Ray and lattice dynamic investigations clearly identified small symmetry breakings and the true space group to be Pm .

We collected thousands of Bragg reflections at selected pressure and temperature values; see details in SI [25].

At 300 K, above the 3-4 GPa transition and up to 12 GPa, our X-Ray data confirm the reported [17] $Cmcm$ space group, as we observed no intensity on forbidden re-

flections (see Fig. 1b).

At 10 K, the data collected at 5 and 12 GPa indicate that the space group cannot be $Cmcm$. Specifically, we observed intensities for i) $H + K$ odd, even for $L = 0$, indicating a break in C centering and of the $\{m_{00z}, \frac{1}{2}\frac{1}{2}\frac{1}{2}\}$ glide mirror and ii) $(H, 0, L)$ with L odd indicating a breaking of the c glide mirror perpendicular to the b axis iii) no intensity on the $(0, 0, L)$ with L odd peaks and iv) a clear monoclinic structure with a significant angle $\approx 103^\circ$ and the unique axis along the c axis of the $Cmcm$. As a consequence the space group for $BaFe_2Se_3$ at high-pressure and low temperature should be either $P2_1/m$ or $P2_1$ with the unique axis along the c axis of the $Cmcm$ (see SI [25] for a detailed symmetry analysis).

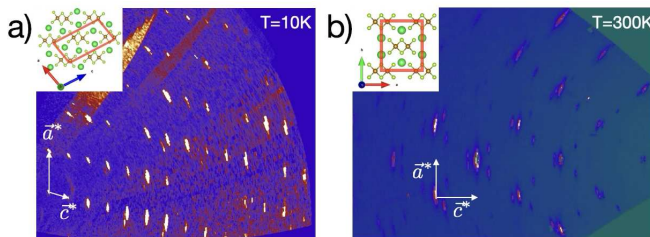


FIG. 1. (Color online) Reconstructions of the reciprocal space at 12 GPa (a) at low temperature in the $(H,0,L)$ plane perpendicular to the ladders in the monoclinic setting and (b) at ambient temperature in the $(H,K,0)$ plane perpendicular to the ladders in the $Cmcm$ setting. Insets show the lattice unit in red with the direct lattice vectors in their respective settings.

We refined the structure for both space groups using JANA software. The refined structures at 5 GPa and 12 GPa at 10 K, in the superconducting phase, are reported in SI [25]. The refinements yielded similar results for both space groups, with agreement factor values (R_{obs}) of 6.81 ($P2_1/m$) and 6.33 ($P2_1$) at 5 GPa, and 3.77 ($P2_1/m$) and 3.76 ($P2_1$) at 12 GPa (see SI for details). Although R_{obs} is marginally better for the $P2_1$ space group, the difference is within the margin of uncertainty, making it unreasonable to definitively assert this space group as the actual space group based on these grounds alone. To resolve this ambiguity, we performed geometry optimisation using DFT. However, similarly to XRD, it was impossible to conclude as no significant energy lowering was observed in the $P2_1$ group. We then examined the lattice dynamics using infrared and Raman spectroscopy, comparing the results with *ab-initio* calculations.

Lattice dynamics. We measured the pressure evolution of the IR reflectivity at 50 K for two configurations of the incident polarization: with the electric field aligned along the a or c direction (in $Cmcm$ notation). In the centrosymmetric $Cmcm$ phase, infrared-active phonons transform according to the B_{1u} , B_{2u} , and B_{3u} irreducible representations. Within the conventional $Cmcm$ setting,

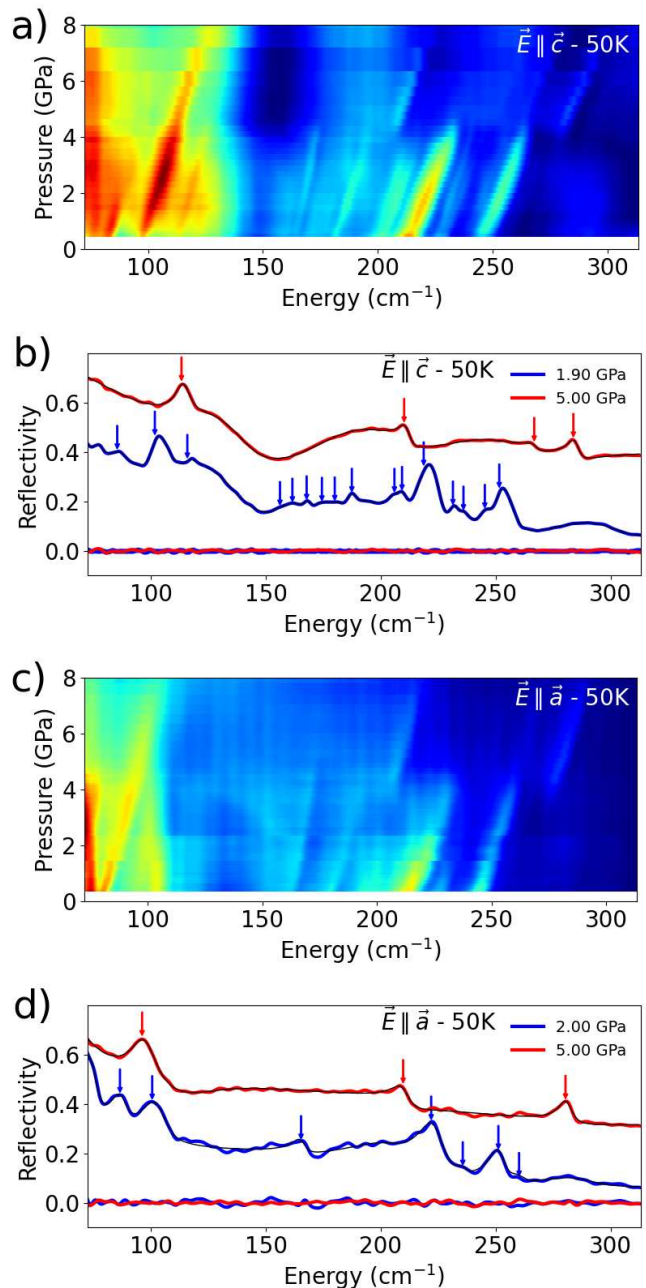


FIG. 2. (Color online) a and c : Reflectivity of $BaFe_2Se_3$ as a function of energy and pressure for $\mathbf{E} \parallel \mathbf{c}$ (B_{1u}) and $\mathbf{E} \parallel \mathbf{a}$ (B_{3u}) in $Cmcm$ setting, respectively. The value of the reflectivity at 310 cm^{-1} has been subtracted to remove the baseline shift due to progressive metallization. Panels b and d show selected reflectivity at 2 GPa (blue line) and 5 GPa (red line) for both polarizations. The fit of the reflectivity is represented by the black line, and the difference between the data and the fit is shown in the corresponding color. Arrows indicate the positions of the fitted phonons.

these modes are associated with electric fields polarized along c (B_{1u}), b (B_{2u}), and a (B_{3u}), respectively. As a consequence, our infrared measurements probe only the

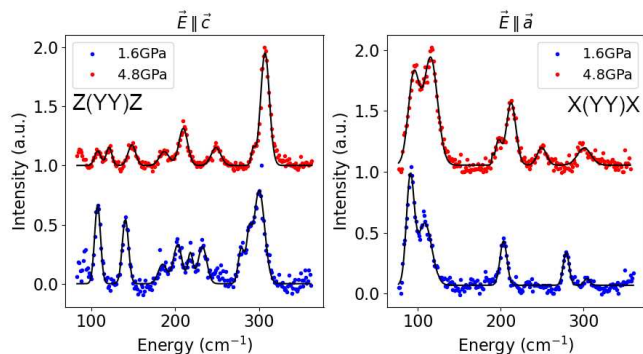


FIG. 3. (Color online) Raman spectra of BaFe_2Se_3 at 1.6 (blue line) and 4.8 GPa (red line) at 300K for both polarizations of the incident light (left : $\mathbf{E} \parallel \mathbf{c}$ corresponding to $Z(\text{YY})Z$; right $\mathbf{E} \parallel \mathbf{a}$ corresponding to $X(\text{YY})X$ with X, Y, Z along a, b, c in $Cmcm$ setting). They belong to A_g irreducible representation in this configuration. The black line correspond to the fit with Gaussian functions.

B_{1u} modes for $\mathbf{E} \parallel \mathbf{c}$ and the B_{3u} modes for $\mathbf{E} \parallel \mathbf{a}$, while the B_{2u} modes polarized along \mathbf{b} are not accessible in our experimental geometry.

At low pressure, we resolved the phonons previously published [20] and observed the expected hardening under pressure up to 4 GPa. It was associated with a decrease in amplitude likely due to the progressive metalization already reported [12].

Above the 4 GPa transition, there is a substantial increase in the optical conductivity, resulting in an elevated baseline for the reflectivity, making it a challenge to discern the phonons. Consequently, only the most intense phonons remain visible and can be fitted. In Fig. 2a and c, we present a map of the reflectivity evolution as a function of pressure, to facilitate the visualization of the phonons and their pressure-induced changes. This approach helps distinguishing phonons from baseline oscillations. The phonons shift in energy with pressure, while the experimental artifacts, such as oscillations, remain at the same energy.

In Fig. 2b and d, we depict the reflectivity at 2 and 5 GPa for both polarizations, fitted with the standard Drude-Lorentz model, where the dielectric function is expressed as the sum of harmonic oscillators [20]. The extracted phonon frequencies are reported in Table I for the 2 GPa and 5 GPa measurements.

At low temperature and high pressure, where the monoclinic symmetry is stabilized, the possible centrosymmetric space group is $P2_1/m$. In this case, infrared-active modes transform as A_u and B_u . For an electric field polarized along \mathbf{c} (defined with respect to the parent $Cmcm$ axes), the infrared-active modes belong to the A_u representation, while for $\mathbf{E} \parallel \mathbf{a}$ they belong to the B_u representation. Raman-active modes in the $P2_1/m$ group transform as A_g and B_g . However, since our Raman mea-

surements are performed in configurations where the incident and scattered light polarizations are parallel, only A_g modes are expected to be observed.

We also performed Raman spectroscopy at ambient temperature. As noted in previous Raman scattering studies on these samples, the signal-to-noise ratio is particularly degraded for this family of systems [27], and it worsens at high pressure due to the increased metallicity. After several attempts, we successfully measured the Raman spectra for two configurations of polarization with both the incoming and outgoing electric fields aligned along the \mathbf{a} and \mathbf{c} directions, respectively, corresponding to the rungs and the legs of the ladders in $Cmcm$ notation.

In the centrosymmetric $Cmcm$ phase relevant at room temperature above 4 GPa, Raman-active phonons belong exclusively to the A_g irreducible representation in our configuration. The mutual exclusion between Raman and infrared activities is lifted in the non-centrosymmetric Pm phase, where phonons can be simultaneously Raman and infrared active. In this latter case, modes polarized along \mathbf{c} transform as A , while modes polarized along \mathbf{a} transform as B .

The Raman spectra at 1.6 and 4.8 GPa are presented in Fig. 3, together with fits using Gaussian functions for each mode. The fitted frequencies, together with their pressure evolution, are reported in the Supplementary Information.

Ab-initio calculations. Phonons calculations were performed for both the $P2_1/m$ and $P2_1$ space groups. The structure was first relaxed under an applied pressure of 6 GPa, starting from the X-ray diffraction structural model (indeed, the 5 GPa calculations did not converge, most probably because the phase transition is close to this pressure in the DFT calculations). The frequencies of the computed lattice dynamics suggest that both structures are dynamically stable. Table I displays the DFT and experimental results in the irreducible representations (irreps) in which we have IR low temperature measurements for comparison. The $\mathbf{E} \parallel \mathbf{c}$ IR measurements correspond to the A_u irrep in the $P2_1/m$ group and A in the $P2_1$ group, while the $\mathbf{E} \parallel \mathbf{a}$ IR measurements correspond to the B_u irrep in the $P2_1/m$ group and B in the $P2_1$ group.

As we can see immediately, in the $P2_1/m$ group the phonon mode at 284 cm^{-1} for $\mathbf{E} \parallel \mathbf{c}$ cannot be assigned to any computed mode, while all modes can easily be assigned in the $P2_1$ group. In fact this mode is close in energy to two A_g mode of the $P2_1/m$ group (see SI), in agreement with the loss of the inversion center. Moreover, although it is less critical, the mode at 267 cm^{-1} for $\mathbf{E} \parallel \mathbf{c}$ deviates, from the last calculated phonon at 252 cm^{-1} , further than the typical uncertainty, which is on the order of 8 cm^{-1} . Finally, despite the fact that the Raman spectra have been measured at 300 K and thus should somewhat deviate from our 0 K calculations, one

TABLE I. Frequencies (cm^{-1}) of optical phonons in the $P2_1/m$ and $P2_1$ space groups, obtained from DFT calculations and IR measurements at 50 K. Only the DFT modes with frequencies above 80 cm^{-1} are listed. See SI for a complete description. The IR mode typed in bold red characters cannot be assigned to any computed one. In the $Cmcm$ setting, c and a are along the leg and the rung of the ladders. The star indicates a phonon visible on the IR raw data (see Fig. 2) but that could not be properly fitted. This value is an estimation leading to larger uncertainty.

$P2_1/m$				$P2_1$			
DFT	IR	DFT	IR	DFT	IR	DFT	IR
A_u	$\mathbf{E} \parallel \mathbf{c}$	B_u	$\mathbf{E} \parallel \mathbf{a}$	A	$\mathbf{E} \parallel \mathbf{c}$	B	$\mathbf{E} \parallel \mathbf{a}$
81		87		80		87	
90		93		85		89	
104		94	96	90		92	
122	113	106		94		95	96
157		132		101		99	
181		139		104		106	
209	210	151		109	113	122	
215		184		122		130	
226		201	210	124		140	
233		233		132		151	
252	267	251		142		157	
	284	269	*266	156		181	
		280	280	179		184	
		298		187		201	
		320		204		210	210
				208	210	217	
				216		227	
				226		233	
				232		251	
				233		268	*266
				252		279	280
				255		299	
				273	267	320	
				275			
				292	284		
				315			

can see that the mode at 197 cm^{-1} for $\mathbf{E} \parallel \mathbf{a}$ cannot be associated to any computed A_g modes (see Fig. 3 and SI).

From all these arguments we can reasonably conclude that the high-pressure low-temperature phase crystallizes in the $P2_1$ group.

Since the high-pressure space group, $P2_1$, is not a subgroup of the ambient-pressure one, Pm , the transition is expected to be first-order. Of course, we cannot exclude the theoretical possibility of an intermediate phase with $P2_1/m$ symmetry in a narrow pressure range. In such a scenario, the structural evolution would proceed via two successive second-order transitions. The first order transition scenario is supported by the observation of

a slight coexistence of phonon modes around 4 GPa in the $\mathbf{E} \parallel \mathbf{a}$ polarization configuration. However, this observation could also be attributed to a pressure gradient within the sample, leading to spatial phase separation and the coexistence of domains corresponding to different structures. The two transitions scenario is supported by the flatness of the energy surface between the $P2_1/m$ and $P2_1$ structures (see Fig. 4). Although the distorted $P2_1$ structure clearly corresponds to an energy minimum, the distortion itself remains weak, with atomic displacements on the order of $\sim 0.005 \text{ \AA}$, comparable to those found in spin-driven multiferroics. Moreover, even for displacements as large as 0.03 \AA , the energy difference remains within a few meV. This suggests that a transition pathway involving two successive second-order transitions is, in principle, possible. Nevertheless, we consider this explanation unlikely, as the coexistence occurs over a pressure range of approximately 0.5 GPa, which exceeds the expected pressure gradient in the cell at such low pressure. In conclusion, although a multi-step transition pathway cannot be ruled out, the most likely scenario remains that the structural transition is first order.

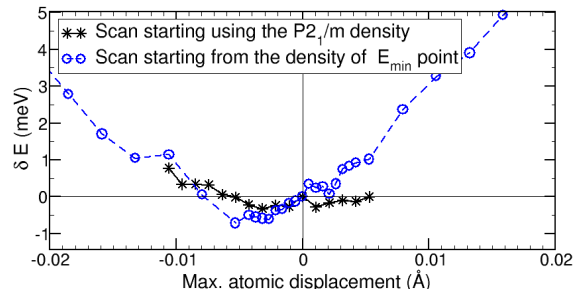


FIG. 4. Energy difference along the soft $P2_1/m$ to $P2_1$ phonons mode. The black curve uses the $P2_1/m$ density as starting point for the self-consistent process, while the blue one uses the density of the minimum energy point of the black curve.

Conclusion. Through a combined experimental and theoretical approach, including X-ray diffraction, infrared and Raman spectroscopies, and *ab-initio* calculations, we have determined the atomic structure of the high-pressure, low-temperature phase of BaFe_2Se_3 in which superconductivity emerges. Our results demonstrate that this phase crystallizes in the polar $P2_1$ space group, establishing BaFe_2Se_3 as a rare example of a quasi-one-dimensional non-centrosymmetric superconductor[33, 34]. The absence of inversion symmetry allows, in the presence of antisymmetric spin-orbit coupling, for the mixing of spin-singlet and spin-triplet pairing channels, among other exotic phenomena [21–23, 35, 36]. In Fe-based systems, where the intrinsic spin-orbit coupling is moderate, such mixing is expected to be limited; nevertheless, broken inversion symmetry

qualitatively alters the allowed superconducting pairing states. These findings provide a well-defined structural foundation for future investigations of superconductivity in reduced dimensionality and highlight BaFe_2Se_3 as a particularly promising platform for exploring the interplay between lattice symmetry, magnetism, and superconductivity in iron-based materials.

Acknowledgment. We thank SOLEIL for synchrotron beam time (Proposal 20210631 and 20220451). V.B. acknowledges the MORPHEUS platform at the Laboratoire de Physique des Solides. This work was financially supported by the ANR COCOM 20-CE30-0029, the France 2030 programme "ANR-11-IDEX-0003" via Integrative Institute of Materials from Paris-Saclay University - 2IM@UPSaclay and by the CSC scholarship (No. 201806830111). M.-B.L., S.D. and G.G. acknowledge the IDRIS high-performance computer center for the calculation time under the GENCI project n°0801842.

* Corresponding author: victor.baledent@universite-paris-saclay.fr

- [1] D. J. Scalapino, A common thread: The pairing interaction for unconventional superconductors, *Reviews of Modern Physics* **84**, 1383 (2012).
- [2] B. Keimer, S. A. Kivelson, M. R. Norman, S. Uchida, and J. Zaanen, From quantum matter to high-temperature superconductivity in copper oxides, *Nature* **518**, 179 (2015).
- [3] G. R. Stewart, Unconventional superconductivity, *Advances in Physics* **66**, 75 (2017).
- [4] G. Stewart, Superconductivity in iron compounds, *Rev. Mod. Phys.* **83**, 1589 (2011).
- [5] R. M. Fernandes, A. V. Chubukov, and J. Schmalian, What drives nematic order in iron-based superconductors?, *Nature Physics* **10**, 97 (2014).
- [6] E. Fradkin, S. A. Kivelson, and J. M. Tranquada, Colloquium: Theory of intertwined orders in high-temperature superconductors, *Reviews of Modern Physics* **87**, 457 (2015).
- [7] D. C. Johnston, The puzzle of high temperature superconductivity in layered iron pnictides and chalcogenides, *Advances in Physics* **59**, 803 (2010).
- [8] A. A. Kordyuk, Iron-based superconductors: Magnetism, superconductivity, and electronic structure (review article), *Low Temperature Physics* **38**, 888 (2012).
- [9] V. Balédent, F. Rullier-Albenque, and D. Colson, Stability of the Fe electronic structure through temperature-, doping-, and pressure-induced transitions in the BaFe_2As_2 superconductors, *Physical Review B* **86**, 235123 (2012).
- [10] V. Balédent, F. Rullier-Albenque, D. Colson, J. M. Ablett, and J. P. Rueff, Electronic properties of BaFe_2As_2 upon doping and pressure: The prominent role of the as p orbitals, *Physical Review Letters* **114**, 1 (2015).
- [11] H. Takahashi, A. Sugimoto, Y. Nambu, T. Yamauchi, Y. Hirata, T. Kawakami, M. Avdeev, K. Matsubayashi, F. Du, C. Kawashima, H. Soeda, S. Nakano, Y. Uwatoko, Y. Ueda, T. J. Sato, and K. Ohgushi, Pressure-Induced Superconductivity in the Iron-Based Ladder Material BaFe_2S_3 , *Nat. Mater.* **14**, 1008 (2015).
- [12] J. Ying, H. Lei, C. Petrovic, Y. Xiao, and V. V. Struzhkin, Interplay of Magnetism and Superconductivity in the Compressed Fe-Ladder Compound BaFe_2S_3 , *Phys. Rev. B* **95**, 241109 (2017).
- [13] H. Lei, H. Ryu, A. I. Frenkel, and C. Petrovic, Anisotropy in BaFe_2Se_3 Single Crystals with Double Chains of FeSe Tetrahedra, *Phys. Rev. B* **84**, 214511 (2011).
- [14] Y. Nambu, K. Ohgushi, S. Suzuki, F. Du, M. Avdeev, Y. Uwatoko, K. Munakata, H. Fukazawa, S. Chi, Y. Ueda, and T. J. Sato, Block Magnetism Coupled with Local Distortion in the Iron-Based Spin-Ladder Compound BaFe_2Se_3 , *Phys. Rev. B* **85**, 064413 (2012).
- [15] M. Mourigal, S. Wu, M. B. Stone, J. R. Neilson, J. M. Caron, T. M. McQueen, and C. L. Broholm, Block Magnetic Excitations in the Orbitally Selective Mott Insulator BaFe_2Se_3 , *Phys. Rev. Lett.* **115**, 047401 (2015).
- [16] H. Hong and H. Steinrück, The crystal chemistry of phases in the Ba-Fe-S and Se systems, *J. Solid State Chem.* **5**, 93 (1972).
- [17] V. Svitlyk, G. Garbarino, A. D. Rosa, E. Pomjakushina, A. Krzton-Maziopa, K. Conder, M. Nunez-Regueiro, and M. Mezouar, High-Pressure Polymorphism of BaFe_2S_3 , *J. Phys. Condens. Matter* **31**, 085401 (2019).
- [18] W.-G. Zheng, V. Balédent, C. V. Colin, F. Damay, J.-P. Rueff, A. Forget, D. Colson, and P. Foury-Leylekian, Universal stripe order as a precursor of the superconducting phase in pressurized BaFe_2Se_3 Spin Ladder, *Communications Physics* **5** (2022).
- [19] W. Zheng, V. Balédent, M. Lepetit, P. Retailleau, E. Elslande, C. Pasquier, P. Auban-Senzier, A. Forget, D. Colson, and P. Foury-Leylekian, Room Temperature Polar Structure and Multiferroicity in BaFe_2Se_3 , *Phys. Rev. B* **101**, 020101 (2020).
- [20] M. J. Weseloh, V. Balédent, W. Zheng, M. Verseils, P. Roy, J. B. Brubach, D. Colson, A. Forget, P. Foury-Leylekian, and M.-B. Lepetit, Lattice dynamics of BaFe_2Se_3 , *J. Phys. Condens. Matter* **34**, 255402 (2022).
- [21] L. P. Gor'kov and E. I. Rashba, Superconducting 2d system with lifted spin degeneracy, *Physical Review Letters* **87**, 037004 (2001).
- [22] K. V. Samokhin, Spin susceptibility of noncentrosymmetric superconductors, *Physical Review B* **76**, 094516 (2007).
- [23] M. Smidman, M. B. Salamon, H. Q. Yuan, and D. F. Agterberg, Superconductivity and spin-orbit coupling in non-centrosymmetric materials: a review, *Rep. Prog. Phys.* **80**, 036501 (2017).
- [24] W. G. Zheng, V. Balédent, L. Bocher, A. Forget, D. Colson, and P. Foury-Leylekian, Origin of spin-glass-like magnetic anomaly in the superconducting and multiferroic spin ladder BaFe_2Se_3 , *Physical Review B* **107**, 024423 (2023).
- [25] See Supplemental Information, containing results of the different X-ray diffraction refinements performed at selected pressure and temperature, a table of fitted frequencies from Raman and infrared spectroscopies, and details on the DFT calculations.
- [26] G. Shen, Y. Wang, A. Dewaele, C. Wu, D. E. Fratanduono, J. Eggert, S. Klotz, K. F. Dziubek, P. Loubeyre, O. V. Fat'yanov, P. D. Asimow, T. Mashimo, and R. M. Wentzcovitch, Toward an international practical pressure scale: A proposal for an IPPS ruby gauge (IPPS-

- Ruby2020), *High Pressure Research* **40**, 299 (2020).
- [27] Z. V. Popović, M. Šćepanović, N. Lazarević, M. Opačić, M. M. Radonjić, D. Tanasković, H. Lei, and C. Petrovic, Lattice dynamics of BaFe_2X_3 ($X = \text{S}, \text{Se}$) compounds, *Phys. Rev. B* **91**, 1 (2015).
- [28] A. D. Becke, Density-functional thermochemistry. III. The role of exact exchange., *J. Chem. Phys.* **98**, 5648 (1993).
- [29] D. Vilela Oliveira, J. Laun, M. F. Peintinger, and T. Bredow, BSSE-correction scheme for consistent gaussian basis sets of double-and triple-zeta valence with polarization quality for solid-state calculations, *J. Comp. Chem.* **40**, 2364 (2019).
- [30] M. Kaupp, P. v. R. Schleyer, H. Stoll, and H. Preuss, Pseudopotential approaches to Ca, Sr, and Ba hydrides. Why are some alkaline earth MX_2 compounds bent?, *J. Chem. Phys.* **94**, 1360 (1991).
- [31] J. Heyd, J. E. Peralta, G. E. Scuseria, and R. L. Martin, Energy band gaps and lattice parameters evaluated with the Heyd-Scuseria-Ernzerhof screened hybrid functional, *J. Chem. Phys.* **123**, 174101 (2005).
- [32] A. Erba, J. K. Desmarais, S. Casassa, B. Civalleri, L. Donà, I. J. Bush, B. Searle, L. Maschio, L. Edith-Daga, A. Cossard, C. Ribaldone, E. Ascrizzi, N. L. Marana, J.-P. Flament, and B. Kirtman, Crystal23: a program for computational solid state physics and chemistry, *J. Chem. Theory Comput.* **19**, 6891 (2022).
- [33] J. K. Bao, J. Y. Liu, C. W. Ma, Z. H. Meng, Z. T. Tang, Y. L. Sun, H. F. Zhai, H. Jiang, H. Bai, C. M. Feng, Z. A. Xu, and G. H. Cao, Superconductivity in quasi-one-dimensional $\text{K}_2\text{Cr}_3\text{As}_3$ with significant electron correlations, *Phys. Rev. X* **5**, 10.1103/PhysRevX.5.011013 (2015).
- [34] Žiga Gosar, T. Arh, K. Jaksetič, A. Zorko, W. Liu, H. Wu, C. Wang, H. Luetkens, B. Lv, and D. Arčon, The pairing symmetry in quasi-one-dimensional superconductor $\text{Rb}_2\text{Mo}_3\text{As}_3$, *J. Phys. Chem. Solids* **181**, 10.1016/j.jpcs.2023.111478 (2023).
- [35] S. Yip, Noncentrosymmetric superconductors, *Annual Review of Condensed Matter Physics* **5**, 15 (2014).
- [36] F. Kneidinger, E. Bauer, I. Zeiringer, P. Rogl, C. Blaas-Schenner, D. Reith, and R. Podloucky, Superconductivity in non-centrosymmetric materials, *Phys. C: Supercond. Appl.* **514**, 388 (2015).

BaFe₂Se₃: a quasi-unidimensional non-centrosymmetric superconductor

Supplemental Information

S. Deng*,¹ A. Roll*,^{2,3} W. G. Zheng*,² G. Giri,^{1,4} T. Vasina,¹ D. Bounoua,³ P. Fertey,⁵ M. Verseils,⁵
C. Bellin,⁶ A. Forget,⁷ D. Colson,⁷ P. Foury-Leylekian,² M.B. Lepetit,^{8,1} and V. Balédent^{2,9,10}

¹*Institut Laue Langevin, 38000 Grenoble, France*

²*Université Paris-Saclay, CNRS, Laboratoire de Physique des Solides, 91405, Orsay, France.*

³*Université Paris-Saclay, CNRS-CEA, Laboratoire Léon Brillouin, 91191, Gif sur Yvette, France*

⁴*Current address: Physics Dept., VIT Bhopal University, Bhopal, India*

⁵*Synchrotron SOLEIL, L'Orme des Merisiers, Saint Aubin BP 48, 91192, Gif-sur-Yvette, France*

⁶*Université Pierre et Marie Curie, IMPMC, CNRS UMR7590, 4 Place Jussieu, 75005 Paris, France*

⁷*Université Paris-Saclay, CEA, CNRS, SPEC, 91191, Gif-sur-Yvette, France.*

⁸*Institut Néel, CNRS, 38042 Grenoble, France*

⁹*Institut universitaire de France (IUF)**

^{10*}*These authors contributed equally to this work.*

(Dated: February 20, 2026)

SYMMETRY ANALYSIS

The general reflection conditions in the $Cmcm$ space group are provided in Table I

TABLE I. Reflection conditions in the $Cmcm$ space group.

hkl : h+k=2n		
0kl : k=2n	h0l : h,l=2n	hk0 : h+k=2n
h00 : h=2n	0k0 : k=2n	00l : l=2n

As the $Cmcm$ space group is C -centered, its unit cell therefore contains two primitive unit cells. The $Cmcm$ conventional unit cell and the primitive one are related as follow

$$\mathbf{a}_P = \frac{1}{2}(\mathbf{a}_C + \mathbf{b}_C) \quad (1)$$

$$\mathbf{b}_P = \frac{1}{2}(-\mathbf{a}_C + \mathbf{b}_C) \quad (2)$$

$$\mathbf{c}_P = \mathbf{c}_C \quad (3)$$

$$\mathbf{a}_P^* = \mathbf{a}_C^* + \mathbf{b}_C^* \quad (4)$$

$$\mathbf{b}_P^* = -\mathbf{a}_C^* + \mathbf{b}_C^* \quad (5)$$

$$\mathbf{c}_P^* = \mathbf{c}_C^* \quad (6)$$

$$h_C = h_P - k_P \quad (7)$$

$$k_C = h_P + k_P \quad (8)$$

$$l_C = l_P \quad (9)$$

where the subscripts P refers to the primitive unit cell and C to the conventional.

Let us analyze what the diffraction pattern of BaFe₂Se₃ at 10 K and 5 or 10 GPa tells us (see Fig.1 of main paper).

- We observe intensity on the h_C, k_C, l_C : $h_C + k_C = 2n + 1$ peaks, including on the $l_C = 0$ ones.
As the C -centering implies $h_C + k_C = 2h_P$, $h_P \in \mathbb{Z}$, the partial translation associated to the C -centering is lost. The primitive unit cell of the true space group is therefore the conventional $Cmcm$ one, which is twice the primitive one, and the true group should be a $Cmcm$ subgroup of k -index=2.
- We observe intensity on the $h_C, 0, l_C$: $l_C = 2n + 1$ peaks.
As the c symmetry operation $\{m_{010}|00\frac{1}{2}\}$ implies $h_C, 0, l_C$: $l_C = 2n$, this symmetry operation does not belong to the true space group.
- When it comes to the $(0, 0, l_C)$ reflexions, there is no sign of intensity on any $l_C = 2n + 1$ peak. Even though not seen any intensity is not a strong proof, one can safely suppose that the $2_1 \{2_{001}|00\frac{1}{2}\}$ symmetry operation is present in the true space group.
- The diffraction pattern pictured in Fig.1 of the main paper clearly shows that the true structure should be monoclinic and not orthorhombic, with a unique axis along the \mathbf{c} $Cmcm$ direction.,

Taking off the C -centering and the $c : \{m_{010}|00\frac{1}{2}\}$ mirror from the generators of $Cmcm$, only five subgroups keep the $2_1 : \{2_{001}|00\frac{1}{2}\}$ screw axis. Out of them only two are monoclinic, namely

- $P2_1/m$ with symmetry operations $\{1|0\}, \{2_{001}|00\frac{1}{2}\}, \{-1|0\}, \{m_{001}|00\frac{1}{2}\}$;
- and $P2_1/c$ with symmetry operations $\{1|0\}, \{2_{001}|00\frac{1}{2}\}, \{-1|\frac{1}{2}\frac{1}{2}0\}, \{m_{001}|\frac{1}{2}\frac{1}{2}\frac{1}{2}\}$.

The $c : \{m_{001}|\frac{1}{2}\frac{1}{2}\frac{1}{2}\}$ mirror implies the following reflection conditions $h_C, k_C, 0 : k_C + k_C = 2n$. As we observe intensity on the $h_C, k_C, 0 : k_C + k_C + 2n + 1$ peaks, the only possible space groups for BaFe_2Se_3 under pressure and at low temperature are $P2_1/m$ and its subgroups.

X-RAY DIFFRACTION

For x-ray diffraction, a diamond anvil cell (DAC) with 600 μm culets was used, with a sample chamber of 300 μm of diameter and 50 μm thick. Several small crystals (about 40 μm of size) were loaded together with a small amount of gold powder and a ruby chip to measure the pressure. The presence of several crystals increases the chances of having a good quality crystal that resists pressure. Helium was used as pressure transmitting medium. Low temperature X-ray diffraction measurements were performed using a newly developed helium circulation cryostat specially designed for diamond anvil cells, which allows for cell rotation at low temperatures, while maintaining the ability to adjust pressure *in situ*. This rotation axis, in conjunction with the cryostat's rotation around a vertical axis, facilitates the collection of a large number of Bragg peaks, thereby improving the completeness of the data sets and the precision of structural refinements. This specialized cryostat is jointly operated by the Laboratoire de Physique des Solides (Orsay, France) and the CRISTAL beamline at the SOLEIL synchrotron (Gif-sur-Yvette, France). The pressure inside the diamond anvil cell was measured using the ruby fluorescence technique, yielding a typical 5% relative accuracy [1]. The pressure measurement was confirmed by the pressure deduced from the gold equation of state and the cell parameter determination of the gold powder sample, also loaded in the DAC chamber. Data collections were conducted at a wavelength of $\lambda = 0.4175 \text{ \AA}$, at the CRISTAL beamline using a 2D detector and processed with the CrysAlis Pro [2].

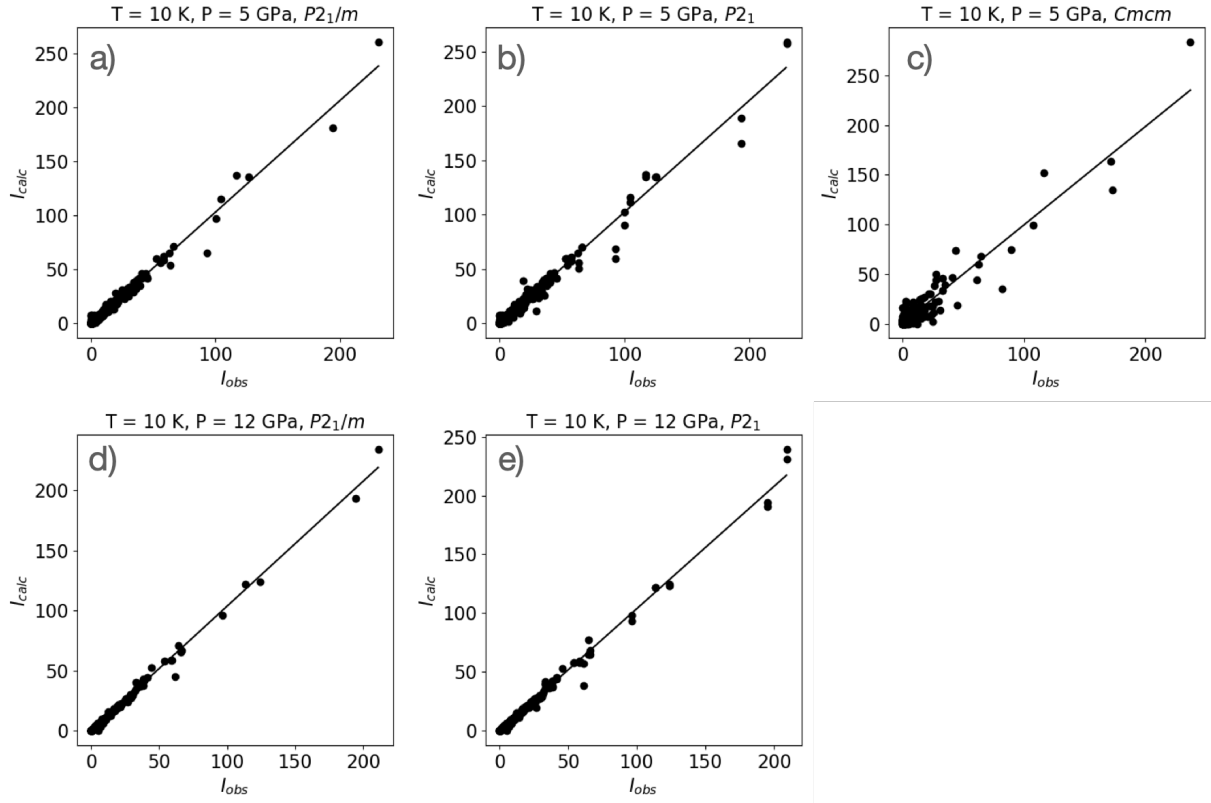
Table II provides the agreement factor values of the refinements ($R(\text{obs})$), as well as the number of peaks used at each measured point of the pressure-temperature phase diagram.

TABLE II. Value of the agreement factors ($R(\text{obs})$) in % for each refinement for selected temperature and pressure. The number in parenthesis corresponds to the number of independent peaks taken into account, with an intensity over noise ratio greater than 3.

Temperature	Pressure	$Pnma$	$Pmn2_1$	Pm	$Cmcm$	$P2_1/m$	$P2_1$
300 K	0 GPa	5.46 (411)	2.18 (619)	1.86 (647)			
	12 GPa	5.47 (625)	4.54 (761)	4.63 (1069)	4.38 (516)	17.52 (1145)	15.87 (1807)
10 K	0 GPa	7.27 (672)	7.08 (936)	7.8 (1419)			
	5 GPa				31.14 (531)	6.81 (1401)	6.33 (1859)
	12 GPa					3.77 (403)	3.76 (690)

For the high-pressure, low-temperature data points (10 K), Fig. 1 compares the calculated versus measured intensities, for the two monoclinic space groups $P2_1/m$ and $P2_1$, and the 5 and 12 GPa pressure values, for which similar refinement quality was obtained. For comparison the same plot is made for $Cmcm$ space group at 5 GPa and 10 K.

FIG. 1. Calculated intensity versus measured intensity at 10 K and at 5 GPa using $P2_1/m$ (a), $P2_1$ (b) and $Cmcm$ (c) space groups, and at 12 GPa using $P2_1/m$ (d) and $P2_1$ (e) space groups.



$P2_1$ at 10 K and 5 GPa

TABLE III. Atomic positions of BaFe_2Se_3 at 10 K and 5 GPa in the $P2_1$ space group ($R=6.33\%$). The lattice parameters are $a=7.211(1)$ Å, $b=5.3402(1)$ Å, $c=14.330(1)$ Å, and $\beta=102.7(1)^\circ$.

Element	x	y	z	U
Ba1	0.7539(3)	0.2501(6)	0.07555(11)	0.0210(10)
Ba2	1.3101(3)	0.2493(5)	0.59099(12)	0.0222(11)
Se1	0.2120(5)	0.2508(10)	0.04479(18)	0.0198(16)
Se2	0.4335(5)	0.2510(9)	0.83419(20)	0.0197(17)
Se3	0.9592(5)	0.2487(9)	0.81804(18)	0.0159(16)
Se4	1.1579(5)	0.7534(10)	0.69454(19)	0.0190(16)
Se5	0.8226(5)	0.2470(11)	0.54096(19)	0.0235(17)
Se6	0.5874(5)	0.7504(9)	0.6593(2)	0.0237(18)
Fe1.1	0.8839(16)	0.5060(10)	0.6792(7)	0.002(5)
Fe1.2	0.125(2)	0.4934(10)	0.3227(9)	0.045(7)
Fe2.1	0.6866(19)	0.5112(9)	0.8114(7)	0.020(5)
Fe2.2	0.315(2)	0.4899(10)	0.1871(8)	0.033(7)

$P2_1$ at 10 K and 12 GPa

TABLE IV. Atomic positions of BaFe_2Se_3 at 10 K and 12 GPa, i.e. in the superconducting phase, in the $P2_1$ space group (R=3.76%). The lattice parameters are $a=6.752(1)$ Å, $b=5.227(1)$ Å, $c=13.866(1)$ Å, and $\beta=103.4(1)$ °.

Element	x	y	z	U
Ba	0.7443(5)	0.2506(8)	0.07123(17)	0.0183(19)
Ba	1.3254(5)	0.2500(7)	0.58658(18)	0.0174(18)
Fe	0.894(3)	0.5002(16)	0.6758(14)	0.004(10)
Fe	0.104(4)	0.501(2)	0.3226(15)	0.032(12)
Fe	0.677(4)	0.5058(19)	0.8072(14)	0.012(12)
Fe	0.303(3)	0.4939(16)	0.1865(15)	0.043(11)
Se	0.2147(8)	0.2535(14)	0.0461(3)	0.015(3)
Se	0.4279(8)	0.2502(13)	0.8345(3)	0.017(3)
Se	0.9702(8)	0.2501(15)	0.8191(3)	0.015(3)
Se	1.1778(8)	0.7474(15)	0.6964(3)	0.013(3)
Se	0.8208(8)	0.2464(13)	0.5353(3)	0.009(3)
Se	0.6089(8)	0.7501(13)	0.6611(3)	0.017(3)

$Cmcm$ at 300 K and 12 GPa

TABLE V. Atomic positions of BaFe_2Se_3 at 300 K and 12 GPa in the $Cmcm$ space group (R=4.38%). The lattice parameters are $a=8.704(1)$ Å, $b=10.453(1)$ Å, and $c=5.260(1)$ Å.

Element	x	y	z	U
Ba	0.5	0.17152(13)	0.25	0.0173(5)
Se	0.5	0.6324(2)	0.25	0.0141(7)
Se	0.20054(8)	0.37143(17)	0.25	0.0189(6)
Fe	0.34977(9)	0.5	0	0.0153(8)

FIG. 2. (Color online)(a) Schematic temperature-pressure phase diagram for the structure of BaFe_2Se_3 . (b-d) Structures of BaFe_2Se_3 in the different space groups obtained in the phase diagram and their respective unit cell for comparison : Pm (a), $Cmcm$ (b) and $P2_1$ (c).

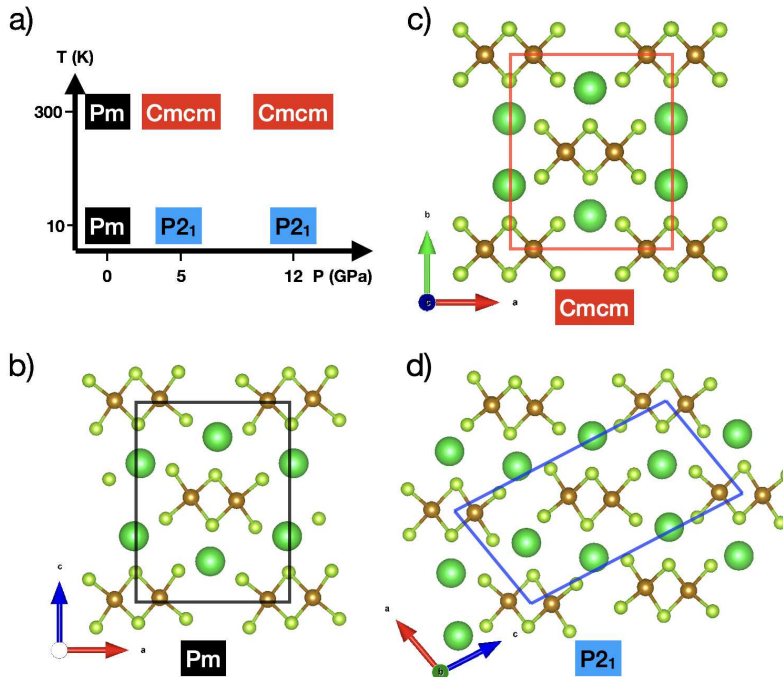


TABLE VI. Fitted phonons frequencies (in cm^{-1}) from infrared reflectivity Raman spectra for both polarization configuration $\mathbf{E} \parallel \mathbf{c}$ and $\mathbf{E} \parallel \mathbf{a}$ in the low pressure phase (1.6, 1.9 or 2 GPa) and high pressure phase (4.8 or 5 GPa) in the $Cmcm$ setting (c and a are along the leg and the rung of the ladder respectively). Error bars from the fit are given within parenthesis. The star indicates phonon visible on the IR raw data but could not be fitted. Its value is an estimation leading to larger uncertainty.

IR (T = 50 K)				Raman (T = 300 K)			
$\mathbf{E} \parallel \mathbf{c}$		$\mathbf{E} \parallel \mathbf{a}$		Y(ZZ)Y ($\mathbf{E} \parallel \mathbf{c}$)		X(ZZ)X ($\mathbf{E} \parallel \mathbf{a}$)	
1.9 GPa	5.0 GPa	2.0 GPa	5.0 GPa	1.6GPa	4.8 GPa	1.6 GPa	4.8 GPa
86(3)	113(3)	87(3)	96(3)	107(1)	108(1)	91(1)	95(1)
102(3)	210(3)	101(8)	210(3)	140(1)	121(1)	108(1)	116(1)
116(3)	267(3)	165(3)	*266(8)	185(1)	148(1)	203(1)	190(1)
156(3)	284(3)	*187(8)	280(3)	203(1)	187(1)	279(1)	197(1)
162(3)		222(3)		218(1)	210(1)	304(1)	213(1)
168(3)		236(3)		232(1)	249(1)		250(1)
174(3)		251(3)		279(1)	293(1)		301(1)
180(3)		260(3)		288(1)	307(1)		
187(3)				300(1)			
206(3)							
209(3)							
219(3)							
231(3)							
236(3)							
245(3)							
252(3)							

DFT CALCULATIONS

The DFT calculations were done using the CRYSTAL23 code [6] that uses atomic gaussian basis set. The locality of the later allows the user of hybrid functionals at low additional computational cost ($\sim 20\%$). The CRYSTAL code also allows a thorough symmetry control as all 230 space group are explicitly coded. Geometry optimizations are done by only using the symmetry allowed distortions of the space group specified in the inputs. Similarly, the phonons modes are computed in the irreps of the specified group.

In order to best account for the electronic correlation at the Fermi level, we used the hybrid B3LYP functional [7]. An atomic gaussian basis of $3\zeta + P$ quality was used for the Fe and Se atoms [8]. The Ba atoms were represented using a relativistic core pseudo-potential of the Stuttgart group [9] and the associated basis set where the diffuse functions exponents were taken as 1.2 as recommended by Scuseria *et al* [10]. The shrinking factors were set to $8 \times 12 \times 4$ resulting in a sampling net of 126 \mathbf{k} -points. The stripe spin ordering found in neutron scattering experiments of BaFe_2Se_3 under pressure [11] was used in all calculations.

TABLE VII. Transverse phonons modes computed using DFT (B3LYP functional) in the $P2_1$ group.

A irrep	B irrep
18	
	35
40	38
48	
49	
55	
57	61
64	65
68	69
	70
	74
	75
76	76
80	
85	87
90	89
	92
94	95
101	99
104	106
109	
122	122
124	
132	130
142	140
	151
156	157
179	181
182	184
204	201
208	210
216	217
226	227
232	
233	233
252	251
255	252
	268
275	279
292	
	299
315	
	320

TABLE VIII. Transverse phonons modes computed using DFT (B3LYP functional) in the $P2_1/m$ group.

A_g irrep	B_g irrep	A_u irrep	B_u irrep
30	33		
42			38
52			48
61		58	58
	65		
68	69		70
73	73		75
78			76
84		81	
	89	90	87
93			93
			94
	99		
104		104	106
108			
	122	122	
128			
132			132
142			139
			151
	157	157	
186	182	181	184
			201
206	210	209	
	215	215	
	227	226	
234	233	233	234
256	254	252	251
274			269
277			280
291			
			298
314			
			320

* Corresponding author: victor.baledent@universite-paris-saclay.fr

- [1] G. Shen, Y. Wang, A. Dewaele, C. Wu, D. E. Fratanduono, J. Eggert, S. Klotz, K. F. Dziubek, P. Loubeyre, O. V. Fat'yanov, P. D. Asimow, T. Mashimo, and R. M. Wentzcovitch, Toward an international practical pressure scale: A proposal for an IPPS ruby gauge (IPPS-Ruby2020), *High Pressure Research* **40**, 299 (2020).
- [2] Rigaku Oxford Diffraction 2016 *CrysAlisPro* Software system, version 1.171.41.64.93a (Oxford: Rigaku Corporation).
- [3] N. Tateiwa and Y. Haga, Evaluations of pressure-transmitting media for cryogenic experiments with diamond anvil cell, *Review of Scientific Instruments* **80**, 10.1063/1.3265992 (2009), arXiv:1001.0454.
- [4] P. Roy, M. Rouzières, Z. Qi, and O. Chubar, The ailes infrared beamline on the third generation synchrotron radiation facility soleil, *Infrared Physics and Technology* **49**, 139 (2006), international Workshop on Infrared Microscopy and Spectroscopy with Accelerator-Based Sources.
- [5] A. Celeste, F. Borondics, and F. Capitani, Hydrostaticity of pressure-transmitting media for high pressure infrared spectroscopy, *High Pressure Research* **39**, 608 (2019).
- [6] A. Erba, J. K. Desmarais, S. Casassa, B. Civalleri, L. Donà, I. J. Bush, B. Searle, L. Maschio, L. Edith-Daga, A. Cossard, C. Ribaldone, E. Ascrizzi, N. L. Marana, J.-P. Flament, and B. Kirtman, Crystal23: a program for computational solid state physics and chemistry, *J. Chem. Theory Comput.* **19**, 6891 (2022).
- [7] A. D. Becke, Density-functional thermochemistry. III. The role of exact exchange., *J. Chem. Phys.* **98**, 5648 (1993).
- [8] D. Vilela Oliveira, J. Laun, M. F. Peintinger, and T. Bredow, BSSE-correction scheme for consistent gaussian basis sets of double-and triple-zeta valence with polarization quality for solid-state calculations, *J. Comp. Chem.* **40**, 2364 (2019).
- [9] M. Kaupp, P. v. R. Schleyer, H. Stoll, and H. Preuss, Pseudopotential approaches to Ca, Sr, and Ba hydrides. Why are some alkaline earth MX_2 compounds bent?, *J. Chem. Phys.* **94**, 1360 (1991).
- [10] J. Heyd, J. E. Peralta, G. E. Scuseria, and R. L. Martin, Energy band gaps and lattice parameters evaluated with the Heyd-Scuseria-Ernzerhof screened hybrid functional, *J. Chem. Phys.* **123**, 174101 (2005).
- [11] W.-G. Zheng, V. Baledent, C. V. Colin, F. Damay, J.-P. Rueff, A. Forget, D. Colson, and P. Foury-Leylekian, Universal stripe order as a precursor of the superconducting phase in pressurized BaFe_2Se_3 Spin Ladder, *Communications Physics* **5** (2022).